The Canadian Mineralogist
Vol. 43, pp. 225-239 (2005)

CARBONATED SERPENTINITE (LISTWANITE) AT ATLIN, BRITISH COLUMBIA: A GEOLOGICAL ANALOGUE TO CARBON DIOXIDE SEQUESTRATION

LYLE D. HANSEN[§] AND GREGORY M. DIPPLE

Department of Earth and Ocean Sciences, University of British Columbia, 3669 Stores Road, Vancouver, British Columbia V6T 1Z4, Canada

TERRY M. GORDON

Department of Geology and Geophysics, University of Calgary, 2500 University Drive Northwest, Calgary, Alberta T2N 1N4, Canada

DAWN A. KELLETT

Department of Earth and Ocean Sciences, University of British Columbia, 3669 Stores Road, Vancouver, British Columbia V6T 1Z4, Canada

ABSTRACT

Listwanite, a carbonate-altered serpentinite commonly associated with gold and mercury mineralization, also represents a natural analogue to CO_2 sequestration *via in situ* carbonation of minerals. The reaction pathways and permeability structure controlling listwanite formation are preserved and exposed at Atlin, British Columbia, where listwanite extends tens of meters into surrounding wallrock. The overall mineralogical transformation is the same as that being considered for industrial sequestration of CO_2. In nature, this reaction proceeds *via* subreactions that are fossilized as spatially distinct zones. Serpentine + olivine + brucite reacted with CO_2 to form serpentine + magnesite, then magnesite + talc, and finally magnesite + quartz. These mineralogical transformations are achieved isochemically, except for the volatile species H_2O and CO_2. Although the first stage of the reaction only accounts for about 5–15% of the carbonation potential of serpentinite, it is very widespread, and therefore may have sequestered a significant portion of the total bound CO_2. Moreover, within intact bedrock, the progress of the magnesite + talc reaction generates fracture permeability, which appears to have locally enhanced reaction. The first two reactions combined account for about half of the carbonation potential for serpentinite and have a small associated increase in the volume of solids, which limits porosity loss. They thus hold the greatest promise for *in situ* mineral carbonation. The carbonation reactions are controlled by the activity of CO_2 in the fluid phase. Proponents of industrial mineral-carbonation processes therefore may seek to control the composition of the input gas to preferentially drive carbonation reactions that minimize porosity loss and maximize permeability generation. Magnetite was progressively destroyed during carbonation, which allowed magnetic susceptibility to be used as a proxy for carbonation-reaction progress. It facilitated the mapping of the permeability structure of these systems and delineated subtle variations in reaction progress that might otherwise have gone unnoticed in the field.

Keywords: listwanite, serpentinite, talc, magnesite, CO_2 sequestration, permeability, mineral carbonation, silica–carbonate alteration, carbon management, magnetic susceptibility, reaction progress, Atlin, British Columbia.

SOMMAIRE

La listwanite, une serpentinite carbonatée généralement associée à une minéralisation aurifère et mercurifère, représenterait un analogue naturel de la séquestration du CO_2 *via* la carbonatation *in situ* de minéraux. Le déroulement des réactions et la structure de perméabilité régissant la formation de la listwanite sont préservés et visibles à Atlin, en Colombie-Britannique, où la listwanite est structuralement liée à un système de fractures et de perméabilité, et s'étend sur des dizaines de mètres dans la roche-mère intacte. La transformation minéralogique globale est la même que celle qui est à l'étude pour la séquestration industrielle du CO_2. Dans la nature, cette réaction procède selon des sous-réactions fossilisées sous forme de zones étalées dans l'espace. Serpentine + olivine + brucite réagissent avec le CO_2 pour former serpentine + magnésite, ensuite magnésite + talc, et enfin magnésite + quartz. Ces transformations minéralogiques se déroulent de façon isochimique, exception faite pour les espèces volatiles H_2O et CO_2. Quoique la première étape de la réaction ne rend compte que d'environ 5–15% du potentiel en carbonatation de la serpentinite, il s'agit d'une réaction très répandue, et donc qui aurait pu avoir piégé une proportion importante du CO_2 total. De

§ *E-mail address*: lhansen@eos.ubc.ca

plus, dans la roche-mère intacte, le progrès de la réaction magnésite + talc produit une perméabilité et des fractures, qui semblent avoir promu la réaction localement. Les deux premières réactions ensemble rendent compte d'environ la moitié du potentiel de carbonatation de la serpentinite, et présentent un faible augmentation du volume des solides, ce qui limite la perte en porosité. Les deux premières étapes de la réaction possèdent donc le plus grand espoir pour une carbonatation *in situ*. Les réactions de carbonatation sont régies par l'activité du CO_2 dans la phase fluide. Les exploitants des processus industriels devraient donc chercher à controller la composition de la phase gazeuse ajoutée afin de forcer les réactions de carbonatation qui minimisent la perte en porosité et maximisent la génération de perméabilité. La magnétite a progressivement été détruite au cours de la carbonatation, ce qui nous a permis d'utiliser la susceptibilité magnétique comme indicateur du progrès de la carbonatation. Ceci a facilité la cartographie de la structure des zones de perméabilité dans ces systèmes et a permis la délinéation de variations subtiles en progrès de la réaction qui autrement auraient bien pu nous échapper sur le terrain.

(Traduit par la Réaction)

Mots-clés: listwanite, serpentinite, talc, magnésite, séquestration du CO_2, perméabilité, carbonatation de minéraux, altération en silice–carbonate, gérance du carbone, susceptibilité magnétique, progrès de la réaction, Atlin, Colombie-Britannique.

Introduction

The presence of low-temperature carbonated ultramafic rocks in nature suggests that conditions favorable for mineral carbonation exist at shallow levels of the crust. In mineral carbonation, CO_2 is chemically bound within the structure of a carbonate mineral by reaction with Mg^{2+}or Ca^{2+}-derived from silicate minerals. Fossil analogues to mineral-carbonation systems are common in ultramafic terranes throughout the world and have produced suites of metamorphic rocks composed of serpentine, magnesite, talc and quartz-bearing assemblages. These rocks are known as listwanite (Kashkai & Allakhverdiev 1965) or as products of silica–carbonate alteration (Sherlock *et al*. 1993). Listwanite has historically been studied because it is commonly spatially associated with lode-gold mineralization (*e.g.*, Ash 2001, Schandl & Naldrett 1992, Wittkopp 1983) and mercury. Liswanite metamorphism has generally been considered a highly metasomatic process that leads to wholesale changes in bulk-rock composition (Schandl & Naldrett 1992, Sherlock *et al*. 1993).

Here we document the mineral reactions, geochemical alteration, and the development of permeability accompanying listwanite formation near Atlin, British Columbia. Listwanite is controlled structurally by a preexisting network of faults and fractures, which served as high-permeability pathways for percolation of CO_2-bearing fluid. Evidence for carbonation, indicated by Mg-carbonate minerals, is present for tens of meters into wallrock adjacent to the controlling fractures. The permeability structure of these systems is therefore similar to that of proposed *in situ* systems of mineral carbonation, which would utilize joints and fractures as a permeability network. Pervasive formation of listwanite adjacent to the fracture systems is found to be isochemical in all major chemical species except H_2O and CO_2, and the overall mineralogical transformation involves breakdown of olivine and serpentine (see below for the relevant reactions). These deposits therefore serve as a geological analogue to mineral carbonation as an environmentally important process. The carbonation process is recorded in the form of mineralogical zonation separated by reaction fronts, which permits each reaction to be examined in isolation. Reactions can therefore be examined individually for their potential in CO_2 sequestration and impact on porosity and permeability.

Relevance to Industrial Applications

The carbonation of serpentine and forsterite (Mg-dominant olivine), to stable Mg-carbonate minerals, is of environmental interest because its ability to fix anthropogenic carbon dioxide (Seifritz 1990). Globally, mineral carbonation offers virtually unlimited capacity and the promise of safe, permanent storage of CO_2, with little risk of accidental release (Guthrie *et al*. 2001). Proposed industrial implementation of mineral carbonation includes the capture of CO_2 from a point source such as a coal-fired power plant, and transport by pipeline to a reaction facility for storage. Reaction could occur within an industrial chemical reactor by carbonation of ultramafic rock mined from a quarry. However, this process demands highly efficient and rapid transformation of minerals (O'Connor *et al*. 2001). As an alternative, direct injection of CO_2 into large subsurface ultramafic formations allows for reaction times of tens to hundreds of years (Guthrie *et al*. 2001), in a process known as *in situ* mineral carbonation.

Numerous schemes of magnesium silicate carbonation have been tested in the laboratory (Goff & Lackner 1998, Goldberg *et al*. 2001, O'Connor *et al*. 2001, Wu *et al*. 2001, Zevenhoven & Kohlmann 2001), and all involve chemical reactions such as:

$$\underset{\text{Serpentine}}{Mg_3Si_2O_5(OH)_4} + 3\ CO_2 \Rightarrow 3\ \underset{\text{Magnesite}}{MgCO_3} + 2\ \underset{\text{Quartz}}{SiO_2} + 2\ H_2O \qquad (R_A)$$

$$\underset{\text{Olivine}}{Mg_2SiO_4} + 2\ CO_2 \Rightarrow 2\ \underset{\text{Magnesite}}{MgCO_3} + \underset{\text{Quartz}}{SiO_2} \qquad (R_B)$$

To date, the rate of reaction in the laboratory has been reported to be up to about 80% conversion of serpentine to silica and magnesite in 30 minutes at 155°C and 185 bar (O'Connor *et al*. 2001). However, this is still too sluggish and the process too costly to accommodate industrial CO_2 output within industrial reactors. *In situ* mineral carbonation could proceed at a more leisurely pace; however, there are no reliable mineral carbonation experiments in CO_2 injection systems (Matter *et al*. 2002). Reaction-path modeling predicts that CO_2 injection into serpentine reservoirs (at 250 bars and 60°C) would result in substantial CO_2 sequestration in a few tens of years (Cipolli *et al.* 2004). Moreover, the large increase in the volume of solids (21% for serpentine and 80% for olivine) associated with reactions R_A and R_B may reduce the sequestration capacity of the reservoir by destroying permeability at the injection site.

Geological Setting

The ultramafic rocks at Atlin represent a tectonically emplaced upper mantle section of oceanic lithosphere (Ash & Arksey 1990a), composed predominantly of harzburgite and minor dunite, now mostly transformed to serpentinite and listwanite. Aitken (1959), Ash & Arksey (1990a) and Hansen *et al*. (2004) documented the structural controls of listwanite development (Fig. 1). Listwanite overprints the foliation of the serpentinite formed during ophiolite obduction, indicating that listwanite formation postdates the emplacement of ophiolitic material onto the Stikine and Cache Creek terranes (Ash 1994). The timing of listwanite genesis in the Atlin area is also constrained by ^{40}Ar–^{39}Ar age determination of chromian muscovite to be in the range *ca*. 168–172 Ma (Ash 2001). Further details on the

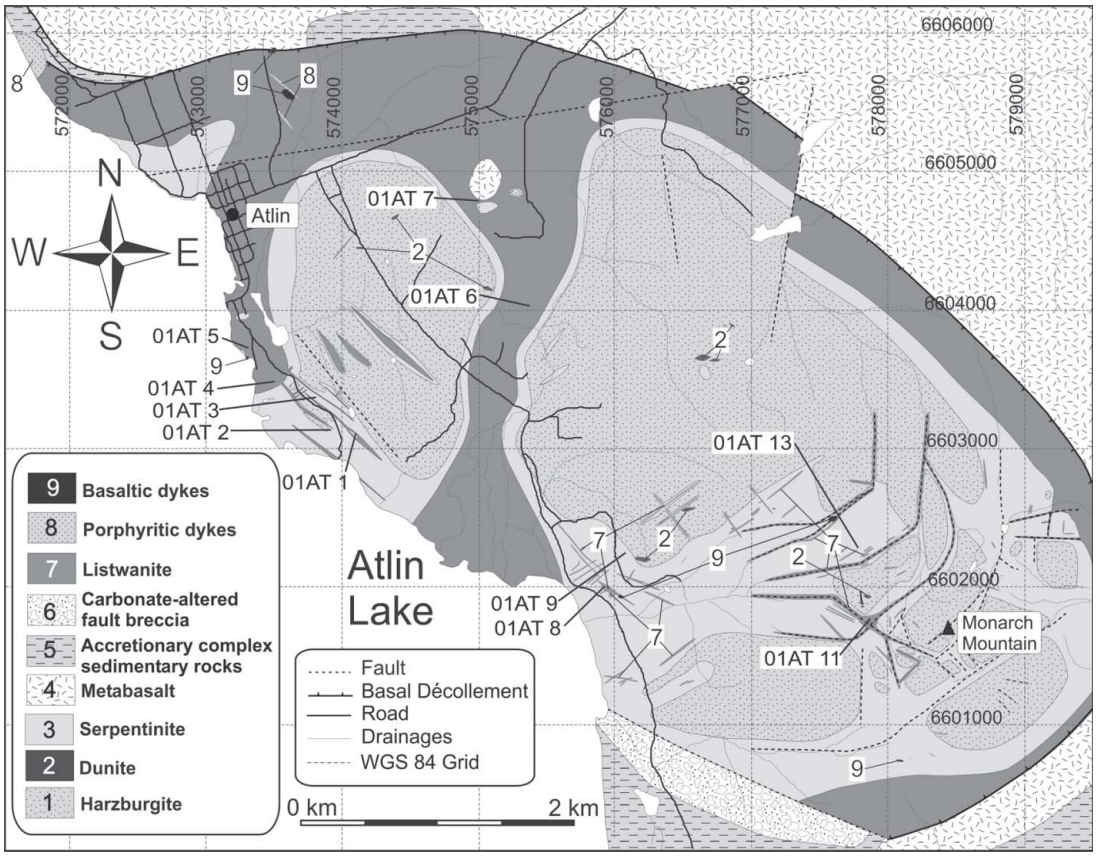

FIG. 1. Simplified geological map of the Atlin area, illustrating the distribution of listwanite along the basal décollement and a joint-and–fracture permeability network, modified from Ash (1994) and Hansen *et al.* (2003).

regional geology near Atlin are provided in Monger (1975, 1977a, b), Monger *et al.* (1978), Bloodgood *et al*. (1989), Ash & Arksey (1990b), Ash *et al*. (1991), Mihalynuk *et al*. (1992) and Ash (1994).

The temperature of formation of listwanite is constrained by fluid-inclusion analysis of quartz–carbonate veins to be in the range of 210–280°C. Homogenization temperatures [$Th_{L–V(L)}$] of 210 to 240°C were measured on low-salinity (<5 wt% equivalent NaCl) fluid inclusions that show no evidence of phase separation (Andrew 1985). Fracture-controlled listwanite likely formed under sublithostatic pressure on the fluid phase, which is assumed to be approximately 500 bars. Listwanite is very common in ultramafic bodies; two other well-known occurrences include the Timmins area of Ontario (*e.g*., Schandl & Naldrett 1992) and the Mother Lode camp in California (*e.g*., Wittkopp 1983). Madu *et al*. (1990) and Schandl & Wicks (1991) reported similar temperatures of formation from other occurrences of listwanite.

Structural Control

Our field mapping confirms the structural control of listwanite development along the basal décollement and along a transecting network of sets of steeply dipping joints and fractures (*e.g.*, Hansen *et al*. 2004, Fig. 1). Although the joint and fracture systems served as the primary conduit for infiltration of CO_2-bearing fluid, pervasive carbonate alteration extends from a few centimeters to many tens of meters outward from the primary structural controls into intact bedrock. The most distal carbonation persists heterogeneously throughout the map area, and cannot be accurately represented at the scale of Figure 1, where only the more focused and intense carbonation is mapped as listwanite. The reaction halos thus extend beyond the area mapped as listwanite, but the spatial distribution of more intensely carbonated rocks serves to illustrate the structural control of fluid infiltration. Mineralogical zonation within the halos is a record of the pathway of the carbonation reaction.

TABLE 1. MINERALOGY OF CARBONATED SERPENTINITE FROM ATLIN, BRITISH COLUMBIA

Sample	Chr	Mgt	Brc	Ol	Srp	Mgs	Tlc	Qtz		CO_2
01AT-8-1	×	×			×				A_1	0.06
01AT-13-1	×	×			×				A_1	0.10
01AT-3-1	×	×	×		×				A_1	0.21
01AT-10-1	×	×	×	×	×				A_1	0.15
01AT-10-2	×	×	×	×	×	×[v]			A_1	0.26
01AT-2-2	×	×	×	×	×				A_1	0.33
01AT-9-1	×	×		×	×	×			R_{1a}	2.10
01AT-11-1	×	×		×	×	×			R_{1a}	2.57
01AT-1-9	×	×			×	×			A_2	3.37
01AT-6-3	×	×			×	×			A_2	4.00
01AT-1-8	×	×			×	×			A_2	4.60
01AT-13-2	×	×			×	×			A_2	7.12
01AT-11-2	×	×			×	×			A_2	9.60
01AT-7-3	×	×			×	×	×		R_2	3.40
01AT-1-7	×	×			×	×	×		R_2	7.19
01AT-1-6	×	×			×	×	×		R_2	9.54
01AT-9-2	×				×	×	×		R_2	17.26
01AT-7-1	×					×	×	×	R_3	21.83
01AT-5-4	×	×[y]				×	×	×	R_3	28.01
01AT-1-5	×	×[z]			×[w]	×	×	×	R_3	34.00
01AT-4-1	×					×	×	×	R_3	34.34
01AT-5-2	×					×		×	A_4	35.20
01AT-6-1[z]	×					×		×	A_4	36.19

[v] only occurs in small veins; [w] occurs in small isolated patches; [y] armored relics and late mantling of chromite and pyrite; [z] magnetite in late fractures and late mantling of chromite; [z] sample contains chromian muscovite. The amount of CO_2 is expressed in wt%.

Mineralogical Zonation and Reaction Sequence

The Atlin ultramafic rocks consist of depleted mantle-derived harzburgite formed during the adiabatic extraction of melt beneath a mid-ocean ridge (Ash & Arksey 1990a). The melt-extraction process and serpentinization event(s) have left the residual harzburgite chemically heterogeneous prior to listwanite metamorphism. The variation in modal orthopyroxene is a record of the original heterogeneity of the harzburgite. Serpentinization reactions consumed olivine + orthopyroxene to form serpentine + magnetite. The extent of serpentization generally exceeds 70% by volume. Serpentine pseudomorphs after orthopyroxene are common.

The mineral content of serpentinite and listwanite was determined by X-ray diffraction (XRD) and optical and scanning electron microscopy (Table 1). Serpentine within uncarbonated samples was confirmed as antigorite by XRD and Raman spectroscopy (Rinaudo & Gastaldi 2003). Assemblages of uncarbonated antigorite ± relict olivine, brucite and orthopyroxene were transformed to assemblages containing antigorite, magnesite, talc and quartz. The mineral assemblages track the migration of three carbonation reactions summarized in Figure 2. In sum, these reactions result in the overall transformations recorded in reactions R_A and R_B. The physical separation of the reaction fronts allows each reaction to be examined in isolation. The boundaries separating each mineral assemblage are reaction isograds in the sense of Carmichael (1970).

The most distal carbonation reactions are volumetrically minor and involve the breakdown of relict olivine *via* reaction R_{1a} to antigorite and magnesite (Fig. 3a, assemblage A_2 of Fig. 2):

$$\underset{\text{Olivine}}{34\ Mg_2SiO_4} + 20\ CO_2 + 31\ H_2O \Rightarrow \underset{\text{Antigorite}}{Mg_{48}Si_{34}O_{85}(OH)_{62}} + \underset{\text{Magnesite}}{20\ MgCO_3} \qquad (R_{1a})$$

O'Hanley & Wicks (1995) documented the reaction of olivine to lizardite and the subsequent transformation to antigorite at Cassiar, B.C. We have been unable

to confirm the presence of lizardite in samples subjected to R_{1a}. Lacking evidence to the contrary, we therefore consider all serpentine to be antigorite.

Trace amounts of brucite are present in some A_1 assemblages, but brucite was not found in samples containing magnesite. Carbonation of olivine-bearing samples may therefore also have included the reaction:

$$\underset{\text{Brucite}}{Mg(OH)_2} + CO_2 \Rightarrow \underset{\text{Magnesite}}{MgCO_3} + H_2O \qquad (R_{1b})$$

Coexisting products and reactants of reaction R_{1b} have not been observed in any samples collected from Atlin. For simplicity, reactions R_{1a} and R_{1b} will be considered together as reaction R_1.

Reaction R_1 generally accommodates less than *ca*. 5 wt% CO_2 (Table 1) and is limited in progress by the abundance of olivine (± brucite) prior to carbonation. Formation of magnesite at the expense of olivine (± brucite) can be driven by a modest increase in the activity of CO_2 in the fluid phase with negligible decrease in activity of H_2O (Fig. 4b). Early, distal carbonation of brucite and olivine is consistent with the observed higher reactivity of olivine and brucite relative to serpentine in mineral-carbonation experiments (Guthrie *et al*. 2001, Lackner *et al.* 1995).

The formation of magnesite plus talc (Assemblage A_3) and the destruction of antigorite (Fig. 3b) mark a major front of carbonation and comprises most of the area mapped as listwanite in Figure 1. Carbonation proceeded *via* the reaction:

$$\underset{\text{Antigorite}}{2\ Mg_{48}Si_{34}O_{85}(OH)_{62}} + 45\ CO_2 \Rightarrow$$

$$45\ \underset{\text{Magnesite}}{MgCO_3} + 17\ \underset{\text{Talc}}{Mg_3Si_4O_{10}(OH)_2} + 45\ H_2O \qquad (R_2)$$

which, combined with reaction R_1, accounts for about half of the overall carbonation-potential of the serpentinite rocks at Atlin (up to ~20 wt%, Table 1, Fig. 4a). It also marks a further increase in the CO_2 content of the fluid phase (Fig. 4b). The cores of large listwanite-bearing systems consist of magnesite plus quartz (Assemblage A_4, Fig. 2), which formed by reaction R_3 at the highest activity of CO_2 in the fluid phase (Fig. 4b):

$$\underset{\text{Talc}}{Mg_3Si_4O_{10}(OH)_2} + 3\ CO_2 \Rightarrow 3\ \underset{\text{Magnesite}}{MgCO_3}$$

$$+ 4\ \underset{\text{Quartz}}{SiO_2} + H_2O \qquad (R_3)$$

Thus, the overall transformation of serpentine and olivine to quartz and magnesite is the same as that recorded in reactions R_A and R_B. Total carbonation of serpentinite leads to CO_2 contents in excess of 36 wt% on a whole-rock basis (Table 1). Reactions R_1, R_2 and R_3 record an increase in the activity of CO_2 in an H_2O-rich fluid (Fig. 4b).

Reactions R_1 to R_3 produce magnesite of different compositions that are discernible with back-scattered electron imaging because of differences in mean atomic mass. Energy-dispersion spectroscopy confirms that increasing mean atomic mass is due primarily to an increase in the Fe content of magnesite. Magnesite M_1 formed during reaction R_1 exhibits a euhedral outline with respect to serpentine and is overgrown by magnesite M_2, with a higher Fe content, associated with talc (Fig. 3b). The dark cores to magnesite in Figures 3c and 3d are likewise interpreted to record growth of magnesite M_1 overprinted by magnesite formed by reaction

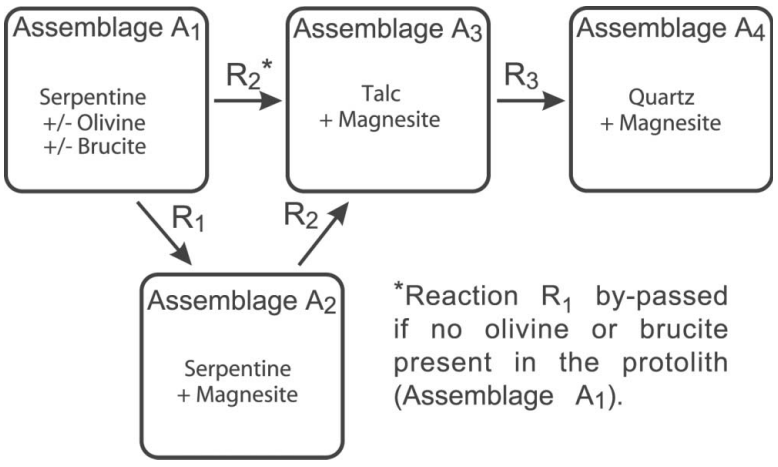

FIG. 2. Simplified flow-chart for the reaction path of the Atlin listwanite system during progressive carbonation of serpentinite.

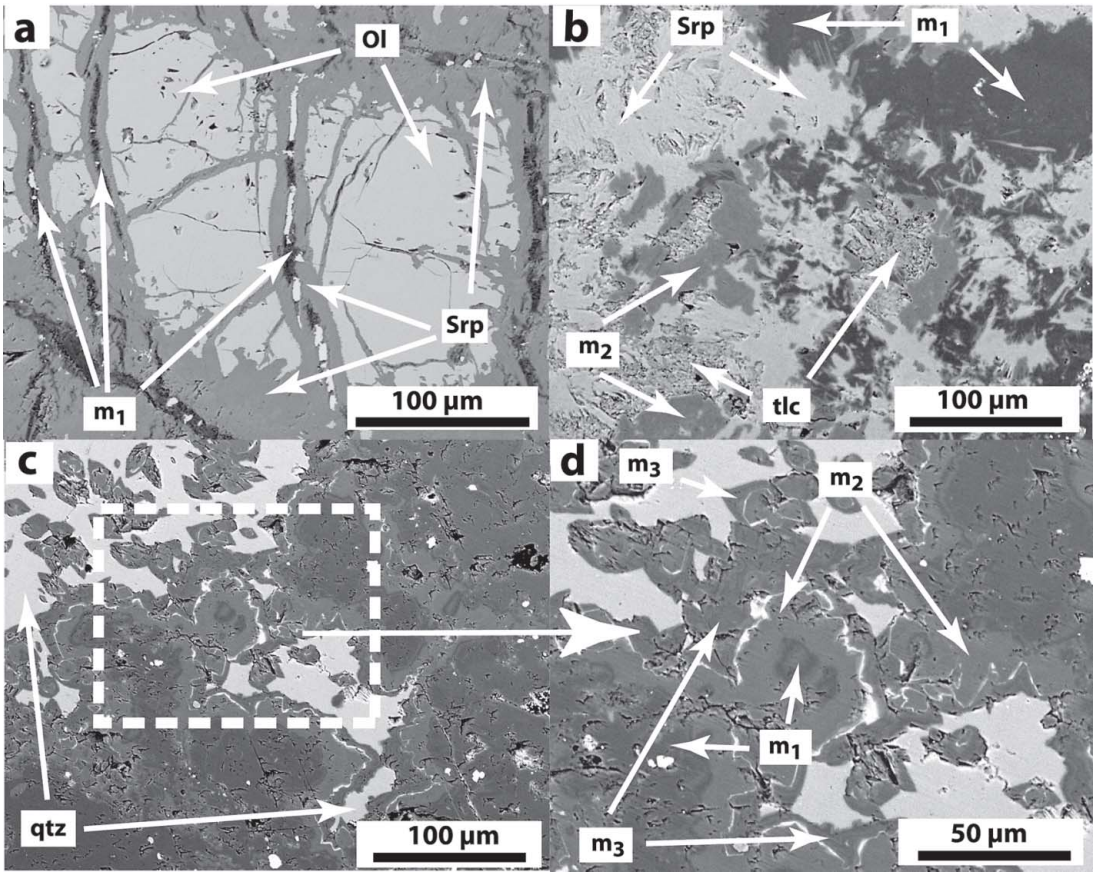

FIG. 3. Back-scattered electron images showing progressive carbonation during listwanite genesis. a) Reaction R_{1b}: olivine to serpentine and magnesite + magnetite. b) Reaction R_2: antigorite to magnesite + talc. c) Reaction R_3: magnesite + quartz assemblage. d) Close-up of (c). M_1, M_2 and M_3 are interpreted to represent magnesite generated during reactions R_1, R_2 and R_3, respectively. Note that magnesite M_2 rims M_1, and that M_3 rims M_2 and forms euhedral boundaries with quartz. Light grey magnesite has a higher mean atomic mass and higher Fe content than dark grey magnesite.

R_2. The dark rim of magnesite M_3 in Figure 3d contains less Fe than magnesite M_2 and has a euhedral outline in contact with quartz.

GEOCHEMICAL CHANGE DURING LISTWANITE FORMATION

The mineralogical transformations in reactions R_1 to R_3 can be achieved through (de)hydration–carbonation reactions without modification of the major oxide chemical composition of serpentinite. Previous investigators of listwanite, however, have argued for pervasive chemical changes accompanying carbonation (Schandl & Naldrett 1992, Sherlock *et al*. 1993, Buisson & LeBlanc 1985). Indeed, the term silica–carbonate alteration that is commonly applied to these systems implies metasomatism. If the mineral reactions at Atlin involve substantial mobility of major non-volatile species, then this system may not serve as a useful analogue for mineral carbonation.

Whole-rock chemical compositions from Atlin (data in the Appendix) are consistent with the hypothesis that carbonation was not accompanied by chemical changes of major non-volatile chemical species. Decreases in wt% MgO and SiO_2, which combined make up about 90% of the non-volatile component of the Atlin rocks, correlate with an increase in CO_2 content at a constant $MgO:SiO_2$ ratio (Fig. 5). This trend is consistent with the immobility and passive depletion of Si and Mg during mass increase (CO_2 addition). Serpentinite and listwanite overlap completely in composition if compositions in terms of major oxides are renormalized to

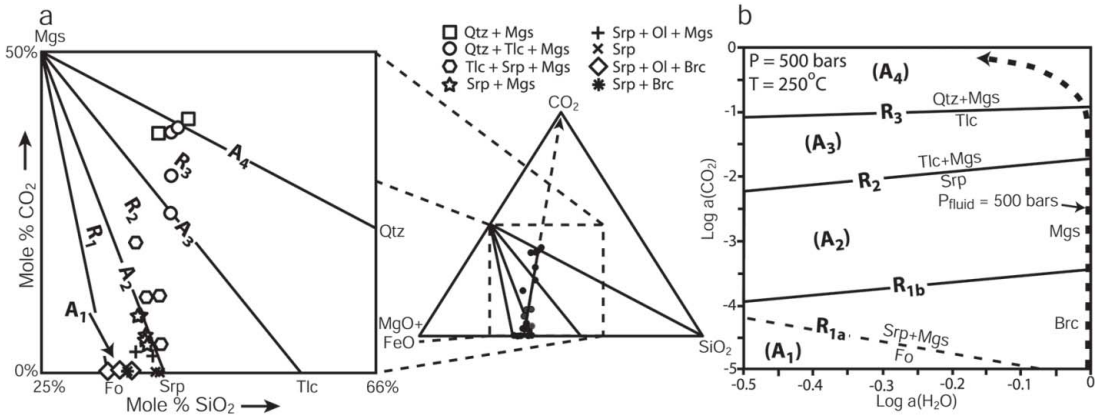

FIG. 4. a) Comparison of the observed mineral content and whole-rock composition in a (MgO + FeO) – SiO_2 – CO_2 diagram projected from H_2O. b) Mineral stability in the system MgO–SiO_2–CO_2–H_2O as a function of activity of H_2O and CO_2 in the fluid phase, calculated using PTAX and the mineral database of Berman (1988). The dashed line is the metastable extension of reaction R_{1a}. The arrowed dashed line is the path of P(fluid) = 500 bars for a binary H_2O–CO_2 fluid, calculated with the CORK equation of state (Holland & Powell 1991).

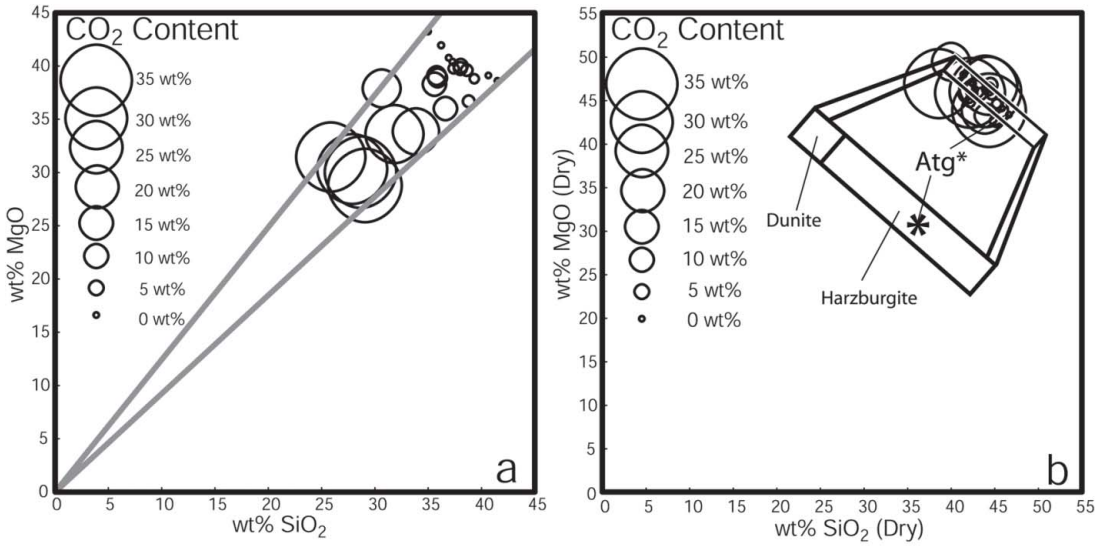

FIG. 5. a) Weight percent MgO plotted *versus* SiO_2. Circle size is proportional to CO_2 content. Data are presented in the Appendix. The observed trend is consistent with the passive dilution of MgO and SiO_2 by increase in CO_2 content. b) MgO and SiO_2 whole-rock compositions are renormalized to 100% (excluding H_2O and CO_2). Carbonated and uncarbonated samples plot on calculated dunite and harzburgite compositions (using Fo_{90} and En_{90} compositions for olivine and orthopyroxene, respectively). Note that the MgO and SiO_2 contents of serpentinite and listwanite are indistinguishable. * Denotes an antigorite-rich rock that contains 7 wt% magnetite (estimated from the data in the appendix) created during the complete serpentinization of (Fo_{90} + En_{90})-rich rocks.

100% excluding H_2O and CO_2 (Fig. 5b). The variation of SiO_2:MgO ratio within the suite of rocks may be a function of the degree of initial serpentinization, or the amount of initial orthopyroxene (Fig. 5b).

Whole-rock geochemical compositions were tested against model sequestration-type reactions R_{1a}, R_{1b}, R_2 and R_3 using the method of Gordon (2003), a new geochemical mass-balance technique that quantitatively

accounts for protolith heterogeneity. The six samples with assemblage A_1 (Table 1) and the lowest CO_2 content (<0.5 wt%; Appendix) were chosen to define the protolith. The protolith for each carbonated rock was modeled as a linear combination of these six samples so that compositional heterogeneities in the protolith do not propagate into the assessment of the carbonation. The remaining samples were divided into three groups. Seven samples without talc or quartz were considered to have experienced only reactions R_{1a} and R_{1b}, four samples with talc but no quartz were considered to have experienced reactions R_{1a}, R_{1b} and R_2, and the remaining six quartz-bearing samples were considered to have experienced the full suite of reactions.

Reaction R_{1a} requires that the model mass-transfer vector for the seven low-CO_2 samples be zero for all species except C and H. For these samples, the model ratio of C added to H added is 20:62. Model reactions R_{1b}, R_2 and R_3 have the ratios of C added to H added of 1:–2, 1:–2 and 3:–2, respectively. A linear algebraic basis (Strang 1993) for the vector space orthogonal to the model mass-transfer vectors (invariant space) can be obtained by simple manipulations using linear algebra. The basis contains linear combinations of elements unaffected by the proposed mass-transfer reactions. Because more than one reaction is involved in each group of samples, the possibility of various extents of reaction of R_{1a}, R_{1b}, R_2 and R_3 means that this method does not constrain the C:H ratio of the mass-transfer vector.

Given the composition of a carbonated rock, the mass-transfer vector must have an origin that can be described by a linear combination of the vectors in protolith space and be orthogonal to vectors in invariant space. This approach provides a vector equation, the least-squares solution of which provides a "best fit" composition of the protolith and "best fit" mass-transfer vector for each carbonated rock.

The success of the model sequestration-type reactions in predicting the observed composition of a modified rock can be judged by comparing the residuals of the least-squares solution with the errors permitted by analytical uncertainties determined from replicate analyses. These results are shown in Figure 6. Positive residuals indicate that the altered rock contains more of

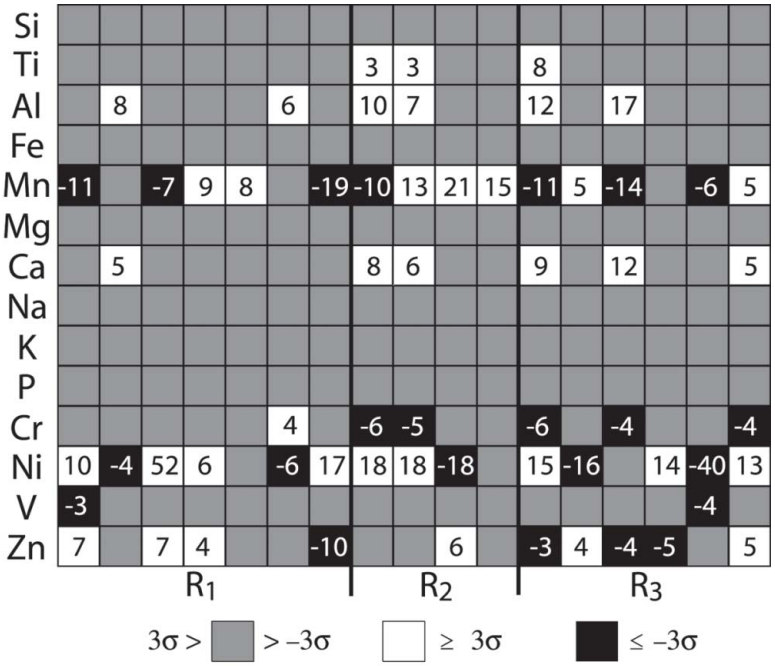

FIG. 6. Ratio of residual error to standard error in whole-rock chemical composition of carbonated samples. Residual error is the difference between compositions predicted by reactions R_1–R_3 and measured compositions. Values of the ratio that exceed three standard errors (positive or negative) indicate an excess or deficiency of the species that cannot be accounted for by the model sequestration-type reactions ($R_{1a\&b}$, R_2 and R_3). In Table B of the Appendix, we list all residuals.

that element than permitted by the hypothesis. In general, the isochemical reaction model provides a good fit to the data. Residuals for Si, Ti, Fe, Mg, Na, K, P, and V return a good to excellent fit, generally within three standard errors (see Appendix). The variation in the composition of these elements in listwanite can be fully explained by the variability of the protolith rocks and the dilution effect of mass addition. The model protolith subspace and simple sequestration-type reactions do not adequately describe the variation in Al, Mn, Ca, Cr, Ni and Zn, which all show large residuals. The failure of the model to explain the compositional variation in these elements is most likely due to inadequate characterization of protolith variability. The residuals are generally both positive and negative and show no systematic variation with degree of carbonation. Moreover, Al, Cr, Ni and Zn are sparingly mobile in hydrothermal systems. There is no convincing evidence for chemical mobility beyond the volatile species, although a more thorough examination of the protolith is required to exclude mobility of Al, Mn, Ca, Cr, Ni and Zn.

Magnetic Susceptibility

Carbonation according to reaction R_1 occurs many tens of meters from major fracture systems but is generally not evident in the field. We have been unable to map the distribution of magnesite formed after olivine breakdown, for example, because this reaction is commonly not discernable in hand sample. The magnetic susceptibility of serpentinite is relatively high because of the formation of magnetite during serpentinization of harzburgite and dunite (*e.g.*, Toft *et al*. 1990). There is also evidence for magnetite generation during reaction R_1 (Fig. 3a). Generally, magnetite forms rim overgrowths on chromite and as disseminated grains aligned in foliation planes and in fractures. Magnetite was subsequently destroyed during carbonation (Table 1) and is completely consumed by the final stages of reaction R_2.

Mass-balance calculations indicate that Fe is conserved during carbonation of serpentinite. Iron liberated by magnetite destruction must therefore be hosted within another mineral. The increase in Fe content of magnesite in M_2 is consistent with conservation of Fe during magnetite destruction. There is a corresponding decrease in whole-rock magnetic susceptibility in samples recording reaction R_2 (Fig. 7).

We have exploited the correlation of whole-rock CO_2 content and magnetic susceptibility (Fig. 7) to develop a semiquantitative measure of reaction progress that can be employed in the field. Magnetic susceptibility of outcrops and hand specimens was measured with an Exploranium KT–9 Kappameter. Although fully carbonated rocks contain >35 wt% CO_2, virtually all magnetic susceptibility appears to have been destroyed by about 20 wt% CO_2, which corresponds to the completion of reaction R_2. The magnetic susceptibility of serpentinite is heterogeneous and reflects the degree of initial serpentinization. A least-squares fit to the data yields a semiquantitative relationship between magnetic susceptibility and CO_2, and thus reaction progress:

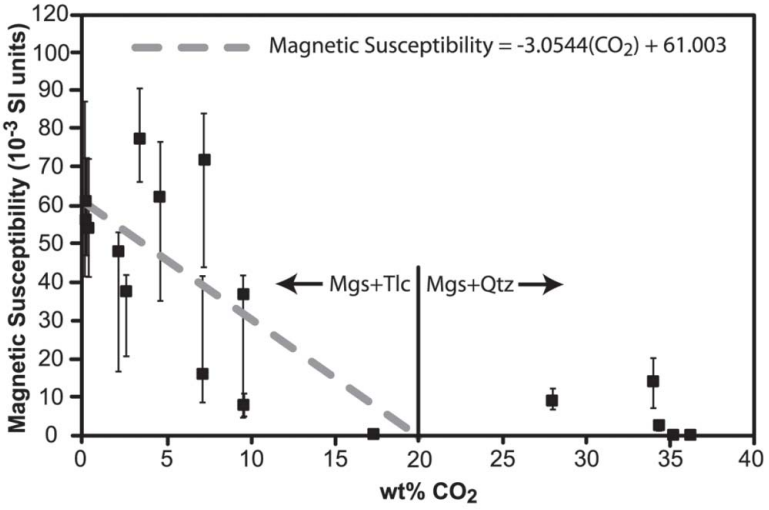

FIG. 7. Magnetic susceptibility *versus* whole-rock wt% CO_2. A linear fit was constrained to intersect zero magnetic susceptibility at 20 wt% CO_2, which approximately marks the maximum CO_2 content of rocks that record complete progress of reaction R_2.

Magnetic Susceptibility (10^{-3} S.I. units) = 61.003 – 3.0544 (wt% CO_2) (Eq_1).

To test the utility of this relationship in mapping reaction progress, a 2 by 2 meter pavement of variably carbonated serpentinite was mapped and analyzed in the field for magnetic susceptibility (approximately 1550 analyses; Fig. 8). Fracture-controlled talc + magnesite + minor serpentine (R_2) intersects the pavements in two discrete zones of reaction that are flanked by distal antigorite + magnesite assemblages (A_2). The mineralogical zonation within the pavement corresponds to discrete changes in magnetic susceptibility. The distinction between serpentinite and rusty serpentinite in the field is very subtle, yet this alteration is prominent in magnetic susceptibility. Measured whole-rock CO_2 content of samples along transect A–B is within 5% of the CO_2 content calculated from magnetic susceptibility and Eq_1 (Fig. 9). Calculated CO_2 content increases continuously within the zone of rusty-weathering serpentinite, implying a gradation in reaction progress across this zone. However, whole-rock geochemistry through the section indicates an abrupt change in CO_2 content (Fig. 9). The gradation in magnetic susceptibility at the reaction front could either reflect the resolution of the magnetic susceptibility meter or the progressive destruction of magnetite not directly linked to progress of carbonation reaction. Regardless, magnetic susceptibility maps provide semiquantitative estimates of reaction progress in the field and are invaluable in discerning the geometry of reaction fronts associated with reaction R_2.

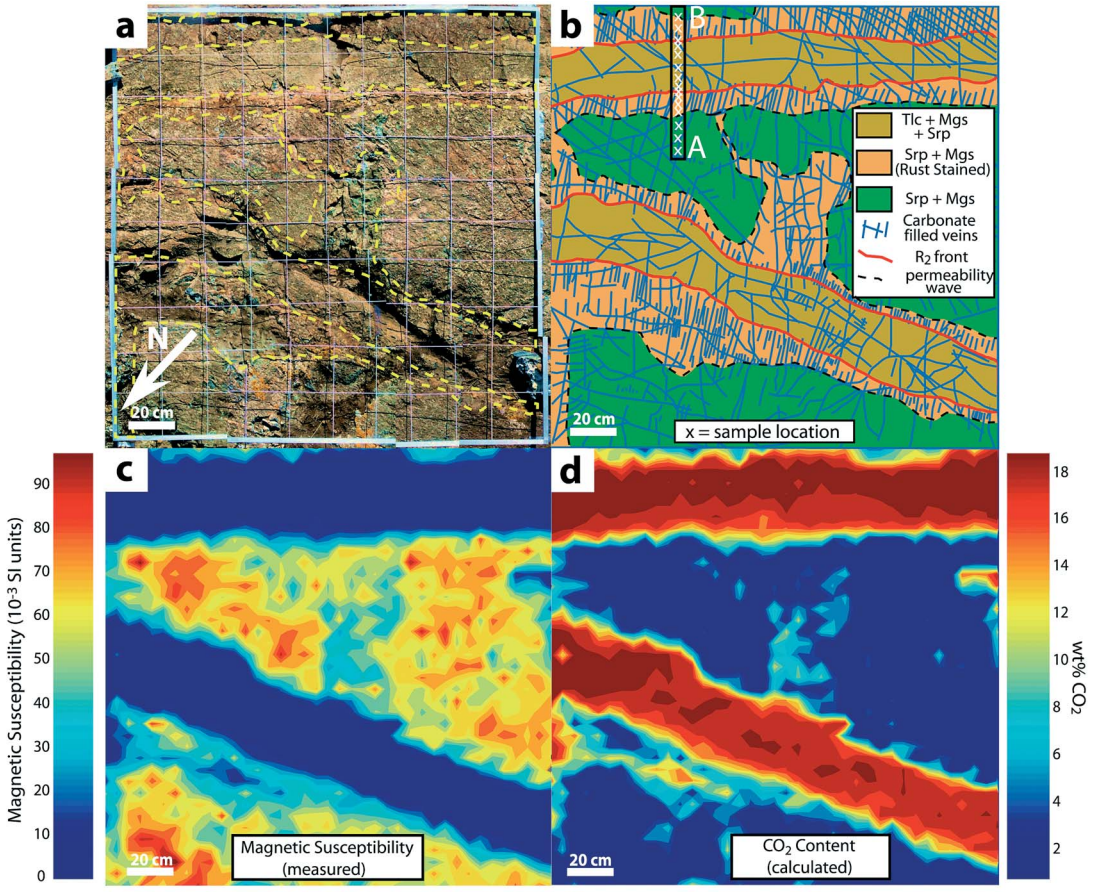

FIG. 8. a) Composite photograph of a 2 by 2 meter pavement-type outcrop on the western slope of Monarch Mountain (E 575887, N 6602098, WGS 84). b) Detailed geological map of the listwanite zone mapped at 1:20 scale. Sample locations and section A–B correspond to those of Figure 9. c) Magnetic susceptibility map, made from *ca.* 1550 measurements, showing the correlation of magnetic susceptibility with mineral content. d) Whole-rock wt% CO_2 map calculated using Eq_1.

Volume Strain Accompanying Reaction

The carbonation reactions involve an increase in the volume of solids (Table 2); each reaction therefore has the potential to create or destroy porosity and permeability. The development of carbonate veins orthogonal to the outer limit of talc plus magnesite reaction in Figures 8a and 8b likely developed in an environment of tension. The mechanical model of Jamtveit *et al*. (2000) predicts the development of high-permeability zones downstream of reactions that produce a net increase in solid volume (Fig. 10). Indeed, the pattern of carbonation and vein formation in Figures 8a and 8b resembles the patterns produced by the Jamtveit *et al*. model. If vein formation outboard of the talc–magnesite reaction front records tension and mechanical coupling of swelling during reaction R_2, then the volume strain of the two processes should balance, at least approximately. Volume strain was calculated by measuring vein thickness (7.6 ± 3.8 mm) and density in the rusty serpentinite zone of Figure 8. The calculated increase in volume of $3.6 \pm 1.8\%$ compares well with the change in solid volume for reaction R_2 (2.3% in a serpentinite rock with 5% relict olivine). The distribution of tension gashes appears to control the outer extent of formation of rusty serpentinite alteration and thus likely has enhanced percolation of reactive fluid into intact wallrock.

Implications for CO_2 Sequestration

Direct carbonation of olivine (± brucite) was previously unrecognized at Atlin and records infiltration and carbonation of intact bedrock many tens to hundreds of meters from the primary system of fracture-controlled permeability. The relative ease with which fluid infiltrated intact bedrock may be due to the inherently high reactivity of olivine and brucite and to the small increase in solid volume associated with carbonation of small amounts of brucite and relict olivine. The extent of reaction R_1 indicates that the primary permeability of serpentinite at Atlin was sufficient for fluid infiltration and progress of R_1. However, the large increase in solid volume of R_1 may limit its usefulness in olivine-rich bedrock. From Table 1, the direct carbonation of brucite and olivine to magnesite plus serpentine accounts for only about 5–15% of the carbonation potential for the serpentinite at Atlin. However, because products of reaction R_1 are widespread, they may have sequestered a significant portion of the total CO_2 content of the listwanite system at Atlin.

The carbonation of antigorite to magnesite and talc binds large quantities of CO_2 with a small associated gain in the volume of solid material. Moreover, within intact bedrock, the progress of this reaction may create a permeability front in advance of the reaction front, further promoting fluid infiltration and reaction. Reactions R_1 and R_2, which combined account for about half of the carbonation potential of serpentinite (Table 1), may hold the greatest promise for *in situ* carbonation of minerals. Complete carbonation of serpentinite to magnesite plus quartz is generally limited to the fractured cores of the largest listwanite systems. Products of reaction R_3 generally are not developed far into intact bedrock, which may have been incapable of accommodating the large increase in solid volume associated with this reaction. Carbonation to magnesite plus quartz thus may limit the sequestration capacity of *in situ* mineral-carbonation systems by destroying porosity and permeability in the vicinity of injection sites. The reaction-path models of Cipolli *et al.* (2004) predict significant conversion of serpentine within *in situ* mineral-carbonation systems to carbonate and "chalcedony" (microcrystalline quartz) within a few tens of years. Their model assumes direct transformation of serpentine to "chalcedony" and magnesite at 250 bars and 60°C on the basis of conditions of the Gruppo di Voltri serpentinite aquifer at Genova. Our investigations at Atlin and Figure 11 suggest that carbonation within the subsurface under these conditions would more likely proceed *via* a series of reactions (R_1 to R_3). Moreover, as indicated above,

TABLE 2. VOLUME CHANGES INCURRED IN THE CARBONATION REACTIONS

Reaction		ΔVs* (rxn)	ΔVs (rock**)
R_{1a}	Ol → Srp + Mgs	55.1%	4.2%
R_{1b}	Brc → Mgs	13.8%	0.4%
R_2	Srp → Tlc + Mgs	2.6%	2.3%
R_3	Tlc → Qtz + Mgs	28.5%	16.2%

* Calculated from the data of Berman (1988) for 250°C and 500 bars.
** Calculated assuming 2.5% brucite and 7.5% relict olivine by volume.

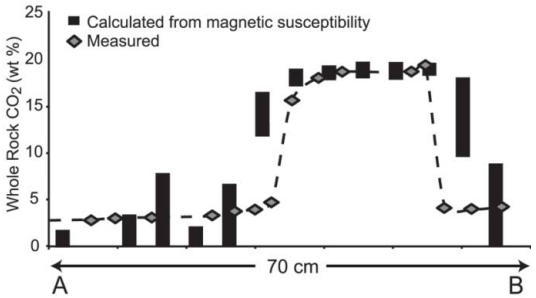

FIG. 9. Measured and calculated wt% CO_2 across A–B from Figure 8b. Wt% CO_2 is calculated using Eq_1 and data on magnetic susceptibility (Fig. 8c). The range in calculated CO_2 content reflects the full range of four measurements of magnetic susceptibility at each location.

reactions R_1 and R_2 involve a relatively small increase in the volume of solids, which will limit the destruction of porosity, yet they still sequester half the CO_2 as complete carbonation to quartz plus magnesite. The stability of carbonation reactions are controlled by the activity of CO_2 in the fluid phase; Figure 11 indicates that the fluid chemistry favorable for driving R_1 and R_2 is a CO_2-rich aqueous fluid. Industrial processes of mineral carbonation could therefore be engineered to control the input gas composition so as to preferentially drive carbonation reactions that minimize porosity loss and maximize permeability generation in the subsurface.

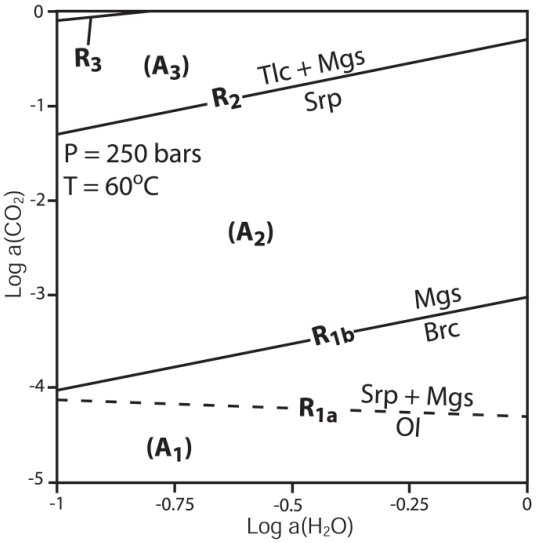

FIG. 11. Mineral stability in the system $MgO–SiO_2–CO_2–H_2O$ as a function of activity of H_2O and CO_2 in the fluid phase, calculated at the Gruppo di Voltri serpentinite aquifer at Genova, Italy (P = 250 bars, T = 60°C; Cipolli *et al.* 2004). The calculations were made using PTAX and the mineral database of Berman (1988).

ACKNOWLEDGEMENTS

This research was funded by a Natural Sciences and Engineering Council of Canada Discovery Grant, by the Oil, Gas and Energy Branch of Environment Canada, and by the Innovative Research Initiative for Greenhouse Gas Mitigation, a program under the Climate Change Action Plan 2000, and administered under Environment Canada and Natural Resources Canada, Earth Sciences Sector. It was conducted under the auspices of Activity 5.3a, "CO_2 storage by mineral carbonation reactions: kinetic and mechanical insights from natural analogues" under the Earth Sciences Sector Climate Change Program, Project CC4500, entitled "Monitoring methods and assessment of carbon sequestration over Canada's landmass". We thank Bill Reynen, Environment Canada for encouraging the initiation of this project, and Mitch Mihalynuk, British Columbia Geological Survey Branch, for his help and expertise at Atlin, including logistics, data sharing, and aerial photography. We have benefitted from many discussions on and off outcrop with Bob Anderson of the Geological Survey of Canada at Vancouver. Carmel Lowe of the Pacific Geoscience Centre first suggested using magnetic susceptibility to map alteration. Kiyoko Kakano provided invaluable field and laboratory assistance, and Sasha Wilson performed Raman analysis. We thank A.E. Williams-Jones, L.P. Baumgartner, D.R.M. Pattison and R.F. Martin for their insights and comments during the review process. We would also like to give special thanks to Dugald Carmichael for his invaluable contributions to the science of metamorphic petrology. Congratulations on your retirement, Dugald!

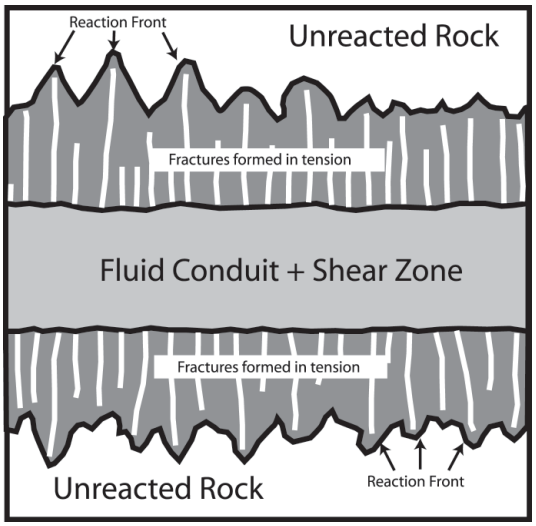

FIG. 10. Distribution of fracture permeability in advance of a reaction, predicted by the mechanical model of Jamtveit *et al*. (2000). In the model, tension-fracture permeability results from an overall increase in solid volume during reaction. Modified from Jamtveit *et al.* (2000).

REFERENCES

AITKEN, J. D. (1959): Atlin map area, British Columbia. *Geol. Surv. Can., Mem*. **307**.

ANDREW, K. (1985): *Fluid Inclusion and Chemical Studies of Gold–Quartz Veins in the Atlin Camp, Northwestern British Columbia*. B.Sc. thesis, Univ. of British Columbia, Vancouver, B.C.

ASH, C.H. (1994): Origin and tectonic setting of ophiolitic ultramafic and related rocks in the Atlin area, British Columbia (NTS 104N). *B.C. Ministry of Energy, Mines and Petroleum Resources, Bull.* **94**.

_____ (2001): Relationship between ophiolites and gold–quartz veins in the North American Cordillera. *B.C. Dep. of Energy, Mines and Petroleum Resources, Bull*. **108**.

_____ & ARKSEY, R.L. (1990a): The Atlin Ultramafic Allochthon: ophiolite basement within the Cache Creek Terrane; tectonic and metallogenic significance (104N/12). *In* Geological Fieldwork 1989. *B.C. Department of Energy and Mines, Pap*. **1990–1**, 365-374.

_____ & _____ (1990b): The listwanite – lode gold association in British Columbia. *In* Geological Fieldwork 1989. *B.C. Department of Energy and Mines, Pap.* **1990–1**, 359-364.

_____, MACDONALD, R.W. & ARKSEY, R.L. (1991): Towards a deposit model for ophiolite related mesothermal gold in British Columbia. *In* Geological Fieldwork 1991. *B.C. Department of Energy and Mines, Pap.* **1992–1**, 253-260.

BERMAN, R.G. (1988): Internally-consistent thermodynamic data for minerals in the system: Na_2O–K_2O–CaO–FeO–Fe_2O_3–Al_2O_3–SiO_2–TiO_2–H_2O–CO_2. *J. Petrol.* **29**, 445-522.

BLOODGOOD, M.A., REES, C.J. & LEFEBURE, D.V. (1989): Geology and mineralization of the Atlin area, northwestern British Columbia (104N/11W and 12E). *In* Geological Fieldwork 1988. *B.C. Department of Energy and Mines, Pap.* **1989–1**, 311-322.

BUISSON, G. & LEBLANC, M. (1985): Gold in carbonatized ultramafic rocks from ophiolite complexes. *Econ. Geol.* **80**, 2028-2029.

CARMICHAEL, D.M. (1970): Intersecting isograds in the Whetstone Lake area, Ontario. *J. Petrol.* **11**, 147-181.

CIPOLLI, G., GAMBARDELLA, B., MARINI, L., OTTONELLO, G. & ZUCCOLINI, M.V. (2004): Geochemistry of high-pH waters from serpentinites of the Gruppo di Voltri (Genova, Italy) and reaction path modeling of CO_2 sequestration in serpentinite aquifers. *Appl. Geochem.* **19**, 787-802.

GOFF, F. & LACKNER, K.S. (1998): Carbon dioxide sequestering using ultramafic rocks. *Environ. Geosci.* **5**(3), 89-101.

GOLDBERG, P., CHEN, Z.Y., O'CONNOR, W.K., WALTERS, R.P. & ZIOCK, H. (2001): CO_2 mineral sequestration studies in US. *Proc. First National Conference on Carbon Sequestration* (*Washington*), *Sess*. **6C**, 10 p.

GORDON, T.M. (2003): Algebraic generalization of the graphical Gresen and Pearce methods for identification of geochemical mass-transfer processes. *Geol. Assoc. Can. – Mineral. Assoc. Can. – Soc. Econ. Geol., Program Abstr.* (*CD-ROM*) **28**, 146 [ISSN 0701–8738, ISBN 0–919216–86–2].

GUTHRIE, G.D., CAREY, J.W., BERGFELD, D., BYER, D., CHIPERA, S., ZIOCK, H. & LACKNER, K.S. (2001): Geochemical aspects of the carbonation of magnesium silicates in an aqueous medium. *Proc. First National Conference on Carbon Sequestration* (*Washington*), *Sess.* **6C**, 14 p.

HANSEN, L.D., DIPPLE, G.M. & ANDERSON, R.G. (2003): Carbonate altered serpentinites of Atlin, BC: a two stepped analogue to CO_2 sequestration. *Geol. Soc. Am., Abstr. Programs* **35**(5), 133-14, 329.

_____, _____, _____ & NAKANO, K.F. (2004): Geologic setting of carbonate metasomatised serpentinite (listwanite) at Atlin, British Columbia: implications for CO_2 sequestration and lode-gold mineralization. *Geol. Surv. Can., Current Research* (in press).

HOLLAND, T & POWELL, R. (1991): A compensated-Redlich–Kwong (CORK) equation for volumes and fugacities of CO_2 and H_2O in the range 1 bar to 50 kbar and 100–1600°C. *Contrib. Mineral. Petrol*. **109**, 265-273.

JAMTVEIT, B., AUSTRHEIM, H. & MALTHE-SORENSSEN, A. (2000): Accelerated hydration of the Earth's deep crust induced by stress perturbations. *Nature* **408**, 75-78.

KASHKAI, A.M. & ALLAKHVERDIEV, I. (1965): *Listwanites: their Origin and Classification*. Akad. Nauk AZ SSR, Inst. Geol., Baku. Russia (in Russ.).

LACKNER, K.S., WENDT, C. H., BUTT, D.P., JOYCE, E.L., JR. & SHARP, D.H. (1995): Carbon dioxide disposal in carbonate minerals. *Energy* **20**, 1153-1170.

MADU, B.E., NESBITT, B.E. & MUEHLENBACHS, K. (1990): A mesothermal gold – stibnite – quartz vein occurrence in the Canadian Cordillera. *Econ. Geol.* **85**, 1260-1268.

MATTER, J.M., TAKAHASHI, T., GOLDBURG, D., MORIN, R.H. & STUTE, M. (2002): Secure, long-term geological carbon sequestration in mafic rocks: results from field and laboratory experiments. *Geol. Soc. Am., Abstr. Programs* **34**(5), 305.

MIHALYNUK, M.G., SMITH, M., GABITES, J.E., RUNKLE, D. & LEFEBURE, D. (1992): Age of emplacement and basement character of the Cache Creek terrane as constrained by new isotopic and geochemical data. *Can. J. Earth Sci.* **29**, 2463-2477.

MONGER, J.W.H. (1975): Upper Paleozoic rocks of the Atlin terrane, northwestern British Columbia and south-central Yukon. *Geol. Surv. Can., Pap.* **74–47**.

_____ (1977a): Upper Paleozoic rocks of northwestern British Columbia. *In* Current Research, Part A. *Geol. Surv. Can., Pap*. **77–1A**, 255-262.

_____ (1977b): Upper Paleozoic rocks of the western Canadian Cordillera and their bearing on the Cordilleran evolution. *Can. J. Earth Sci.* **14**, 1832-1859.

_____, RICHARDS, T.A. & PATERSON, I.A. (1978): The hinterland belt of the Canadian Cordillera: new data from northern and central British Columbia. *Can. J. Earth Sci.* **15**, 823-830.

O'CONNOR, W.K., DAHLIN, D.C., NILSEN, D.N., RUSH, G.E., WALTERS, R.P. & TURNER, P.C. (2001): Carbon dioxide sequestration by direct mineral carbonation: results from studies and current status. *Proc. First National Conference on Carbon Sequestration* (*Washington*), *Sess.* **6C**, 10 p.

O'HANLEY, D.S. & WICKS, F. J. (1995): Conditions of formation of lizardite, chrysotile and antigorite, Cassiar, British Columbia. *Can. Mineral.* **33**, 753-773.

RINAUDO, C., GASTALDI, D. & BELLUSO, E. (2003): Characterization of chrysotile, antigorite and lizardite by FT-Raman spectroscopy. *Can. Mineral.* **41**, 883-890.

SCHANDL, E.S. & NALDRETT, A.J. (1992): CO_2 metasomatism of serpentinites, south of Timmins, Ontario. *Can. Mineral.* **30**, 93-108.

_____ & WICKS, F.J. (1991): Two stages of CO_2 metasomatism at the Munro mine, Munro Township, Ontario: evidence from fluid-inclusion, stable-isotope, and mineralogical studies. *Can. J. Earth Sci.* **28**, 721-728.

SEIFRITZ, W. (1990): CO_2 disposal by means of silicates. *Nature* **345**, 486.

SHERLOCK, R.L., LOGAN, M.A.V. & JOWETT, E.C. (1993): Silica carbonate alteration of serpentinite, implications for the association of precious metal and mercury mineralization in the Coast Ranges. *Soc. Econ. Geol., Guidebook Ser.* **16**, 90-116.

STRANG, G. (1993): *Introduction to Linear Algebra*. Wellesley-Cambridge Press, Wellesley, Massachusetts.

TOFT, P.B., ARKANI-HAMED, J. & HAGGERTY, S.E. (1990): The effects of serpentinization on density and magnetic susceptibility: a petrophysical model. *Phys. Earth Planet. Interiors* **65**, 137-157.

WITTKOPP, R.W. (1983): Hypothesis for the localization of gold in quartz veins, Allegheny district. *California Geol.* **36**(6), 123-127.

WU, J., SHEEN, J., CHEN, S. & FAN, Y. (2001): Feasibility of CO_2 fixation via artificial rock weathering. *Ind. Eng. Chem. Res.* **40**, 3902-3905.

ZEVENHOVEN, R. & KOHLMANN, J. (2001): CO_2 sequestration by magnesium silicate mineral carbonation in Finland. *Second Nordic Minisymposium on Carbon Dioxide Capture and Storage* (*Gotenborg*): http://www.entek.chalmers.se/~anly/symp/symp2001.html.

Received December 8, 2003, revised manuscript accepted September 25, 2004.

APPENDIX

Bulk geochemical samples were crushed and powdered in a tungsten carbide shatterbox. Powders were sent to the Geochemical Laboratories at McGill University, Montreal, Quebec, for bulk analysis by X-ray fluorescence. Results are included in Table A. Samples were examined for major, minor and trace elements, CO_2 content by induction furnace, and total volatile content by loss on ignition (LOI). Standard errors used in calculations were determined from seven blind replicate analysis of one sample. In Table B, we present the ratio of residuals to one standard error for data illustrated in Figure 6.

TABLE A. WHOLE-ROCK GEOCHEMICAL DATA, LISTWANITE SAMPLES FROM ATLIN, BRITISH COLUMBIA

Sample	SiO_2	TiO_2	Al_2O_3	Fe_2O_3	MnO	MgO	CaO	Na_2O	K_2O	P_2O_5	Cr_2O_3	Ni	V	Zn	LOI	Total	CO_2
01AT-8-1	41.50	0.012	0.14	7.99	0.098	38.61	0.02	0.03	0.01	0.012	3617	2191	23	25	11.65	100.66	0.06
01AT-13-1	40.64	0.014	1.19	6.93	0.088	39.12	0.15	<d.l.	0.01	0.010	3154	2196	46	21	11.90	100.57	0.10
01AT-10-1	34.98	0.010	0.09	8.08	0.105	43.25	0.06	<d.l.	0.01	0.010	4274	2637	19	31	13.50	100.77	0.15
01AT-3-1	36.93	0.010	0.23	8.23	0.090	40.78	0.02	0.01	0.01	0.010	3254	2393	23	28	13.94	100.83	0.21
01AT-10-2	37.29	0.010	0.40	7.96	0.113	40.39	0.37	<d.l.	0.01	0.009	4540	2315	31	33	13.14	100.38	0.26
01AT-2-2	36.21	0.010	0.16	7.90	0.099	41.95	0.37	<d.l.	0.01	0.010	4648	2452	20	28	13.16	100.57	0.33
01AT-9-1	39.32	0.012	1.08	6.80	0.085	38.81	0.11	0.06	0.01	0.010	4012	2299	36	39	13.50	100.44	2.10
01AT-11-1	37.38	0.013	1.11	9.15	0.167	39.78	0.44	0.01	0.01	0.012	3778	2220	50	36	12.10	100.78	2.57
01AT-1-9	38.62	0.011	0.27	7.12	0.082	39.62	0.03	0.01	0.02	0.012	4206	2789	17	36	14.10	100.60	3.37
01AT-7-3	38.80	0.017	0.91	7.21	0.140	36.69	1.61	0.02	0.01	0.010	3412	2175	33	28	14.04	100.02	3.40
01AT-6-3	38.01	0.012	0.34	7.03	0.074	39.77	0.06	<d.l.	0.01	0.011	2522	2388	18	25	14.53	100.34	4.00
01AT-1-8	38.05	0.011	0.14	6.58	0.070	40.01	0.06	0.02	0.01	0.010	2861	2389	12	7	14.98	100.47	4.60
01AT-13-2	35.79	0.013	0.92	8.58	0.139	39.10	0.04	0.03	0.01	0.010	5138	2194	32	39	15.35	100.72	7.12
01AT-1-7	35.88	0.011	0.15	8.10	0.083	38.88	0.09	0.11	0.02	0.009	4111	2427	20	12	16.70	100.69	7.19
01AT-1-6	36.62	0.014	1.05	7.78	0.110	36.01	0.97	0.02	0.02	0.009	3375	2214	37	31	17.64	100.81	9.54
01AT-11-2	35.58	0.011	0.22	7.45	0.121	38.29	0.46	<d.l.	0.01	0.009	3969	2004	29	38	17.84	100.59	9.60
01AT-9-2	30.63	0.009	0.07	7.11	0.095	37.90	0.23	<d.l.	0.01	0.009	3216	2250	17	27	23.80	100.40	17.26
01AT-7-1	33.85	0.022	1.09	6.80	0.103	33.85	0.88	0.04	0.01	0.009	3119	2088	41	25	22.91	100.09	21.83
01AT-5-4	31.84	0.008	0.07	5.76	0.066	33.61	0.10	<d.l.	0.01	0.011	3110	1760	<d.l.	23	28.41	100.38	28.01
01AT-1-5	25.86	0.010	0.86	7.21	0.088	31.46	0.90	0.05	0.05	0.008	3185	1938	34	28	33.66	100.67	34.00
01AT-4-1	27.87	0.008	0.14	6.78	0.113	30.33	0.24	<d.l.	0.01	0.008	3926	1956	15	21	34.09	100.18	34.34
01AT-5-2	28.65	0.009	0.07	5.69	0.065	30.03	0.18	0.02	0.01	0.008	3359	1502	<d.l.	17	34.99	100.21	35.20
01AT-6-1	29.07	0.009	0.24	4.79	0.072	28.78	2.06	<d.l.	0.03	0.007	3177	1794	11	41	34.63	100.18	36.19
Standard error	0.09	0.001	0.01	0.04	0.001	0.11	0.01	0.04	0.004	0.001	95	4	2	1	0.05		0.05

Units in wt% except for Cr_2O_3, Ni, V and Zn, concentrations of which are reported in ppm.

TABLE B. RATIO OF RESIDUALS TO ONE STANDARD ERROR FOR DATA ILLUSTRATED IN FIGURE 6

	R1	R1	R1	R1	R1	R1	R1	R2	R2	R2	R2	R3	R3	R3	R3	R3	R3
Si	-3.E-03	-0.15	1.E-03	5.E-04	1.E-04	-0.12	-0.01	-0.21	-0.15	2.E-04	-4.E-05	-0.24	5.E-04	-0.34	9.E-05	-9.E-04	-0.12
Ti	-1.93	1.78	-1.90	-0.40	-1.16	2.05	1.93	3.14	3.08	1.49	0.61	8.11	-2.02	2.24	1.42	0.77	0.32
Al	0.28	7.73	0.01	-0.03	-0.02	6.10	0.33	10.34	7.20	-0.05	-0.02	11.71	-0.04	17.07	4.E-03	0.04	2.92
Fe	0.02	0.78	4.E-03	-0.01	-0.01	0.59	0.05	1.07	0.73	-0.02	-0.01	1.21	-0.01	1.74	3.E-03	0.01	0.63
Mn	-10.56	0.86	-7.46	9.17	8.01	-0.33	-18.99	-10.27	13.44	20.90	14.85	-10.85	5.22	-13.89	-2.30	-5.71	5.09
Mg	-2.E-04	0.03	-1.E-03	-4.E-05	6.E-05	0.02	8.E-04	0.05	0.03	5.E-04	2.E-04	0.05	2.E-04	0.07	-2.E-04	6.E-04	0.03
Ca	-0.40	5.36	-0.15	0.03	0.03	0.83	0.18	8.34	5.91	0.05	0.06	9.44	-0.02	12.31	0.01	-0.04	5.03
Na	0.73	0.04	-0.11	-0.07	-0.01	0.16	1.15	0.13	0.10	-0.03	0.04	0.28	-0.11	0.24	0.00	0.12	0.01
K	0.04	-0.01	1.38	0.02	0.03	0.01	1.41	0.81	0.01	0.07	0.14	0.11	0.18	2.39	0.19	0.51	0.78
P	0.25	1.61	0.08	-0.61	-1.23	1.16	4.E-03	1.08	0.27	-0.44	-0.03	1.13	-0.04	1.09	1.18	-0.56	-0.38
Cr	2.47	-0.98	0.79	-0.37	-0.32	3.52	0.53	-5.54	-4.71	-0.77	-0.59	-6.29	-0.14	-3.68	0.05	0.34	-3.77
Ni	9.75	-3.68	52.21	5.92	2.54	-5.63	16.61	17.53	17.59	-17.12	0.90	14.68	-16.49	2.06	14.20	-39.94	13.36
V	-3.17	-0.28	-1.46	0.74	0.98	-2.03	-2.03	-1.65	0.63	2.76	1.55	-0.41	-0.08	0.64	-2.58	-3.87	0.85
Zn	7.33	-2.98	6.53	4.10	1.01	-1.58	-10.66	-2.92	1.51	6.46	2.71	-3.42	4.31	-3.63	-4.85	-0.60	4.59